Spatial resolution in prism-based surface plasmon resonance microscopy

Loïc Laplatine, Loïc Leroy, Roberto Calemczuk, Dieudonné Baganizi, Patrice Marche, Yoann Roupioz, Thierry Livache

Spatial resolution in prism-based surface plasmon resonance microscopy

Loïc Laplatine,[1,2,3] **Loïc Leroy,**[1,2,3,*] **Roberto Calemczuk,**[1,2,3] **Dieudonné Baganizi,**[1,2,3,4,5] **Patrice N. Marche,**[4,5] **Yoann Roupioz**[1,2,3] **and Thierry Livache**[1,2,3]

[1]*Univ. Grenoble Alpes, INAC-SPRAM, F-38000 Grenoble, France*
[2]*CNRS, INAC-SPRAM, F-38000 Grenoble, France*
[3]*CEA, INAC-SPRAM, F-38000 Grenoble, France*
[4]*Univ. Grenoble Alpes, Institut Albert Bonniot, UMRS U823, F-38000 Grenoble, France*
[5]*INSERM U823, F-38000 Grenoble, France*
[*]*loic.leroy@ujf-grenoble.fr*

Abstract: Several optical surface sensing techniques, such as Surface Plasmon Resonance (SPR), work by imaging the base of a prism by one of its faces. However, such a fundamental optical concern has not been fully analyzed and understood so far, and spatial resolution remains a critical and controversial issue. In SPR, the propagation length L_x of the surface plasmon waves has been considered as the limiting factor. Here, we demonstrate that for unoptimized systems geometrical aberrations caused by the prism can be more limiting than the propagation length. By combining line-scan imaging mode with optimized prisms, we access the ultimate lateral resolution which is diffraction-limited by the object light diffusion. We describe several optimized configurations in water and discuss the trade-off between L_x and sensitivity. The improvement of resolution is confirmed by imaging micro-structured PDMS stamps and individual living eukaryote cells and bacteria on field-of-view from 0.1 to 20 mm^2.

OCIS codes: (240.6680) Surface plasmon; (350.5730) Resolution; (170.1530) Cell analysis; (220.1010) Aberrations (global); (230.5480) Prisms.

References and links

1. R. W. Wood, "On a Remarkable Case of Uneven Distribution of Light in a Diffraction Grating Spectrum," Proc. Phys. Soc. London **18**(1), 269 (1902).
2. A. Otto, "A new method for exciting non-radioactive surface plasma oscillations," Phys.Stat.Sol. **26**, 99–101 (1968).
3. E. Kretschmann, and H. Raether, "Radiative decay of nonradiative surface plasmons excited by light," Z. Naturforsch. A **23**, 2135 (1968).
4. J. Homola, "Electromagnetic Theory of Surface Plasmons," in *Surface Plasmon Resonance Based Sensors* (Springer Berlin Heidelberg, 2006).
5. J. Homola, "Surface plasmon resonance sensors for detection of chemical and biological species," Chem. Rev. **108**(2), 462–493 (2008).
6. P. N. Abadian, C. P. Kelley, and E. D. Goluch, "Cellular Analysis and Detection Using Surface Plasmon Resonance Techniques," Anal. Chem. **86**(6), 2799–2812 (2014).
7. S. Milgram, R. Bombera, T. Livache, and Y. Roupioz, "Antibody microarrays for label-free cell-based applications," Methods. **56**(2), 326–333 (2012).
8. S. Bouguelia, Y. Roupioz, S. Slimani, L. Mondani, G. Casabona, C. Durmort, T. Vernet, R. Calemczuk, and T. Livache, "On-chip microbial culture for the specific detection of very low levels of bacteria," Lab. Chip **13**(20), 4024–4032 (2013).

#214954 - $15.00 USD Received 27 Jun 2014; revised 22 Aug 2014; accepted 22 Aug 2014; published 11 Sep 2014

9. Y. Yanase, T. Hiragun, S. Kaneko, H. J. Gould, M. W. Greaves, and M. Hide, "Detection of refractive index changes in individual living cells by means of surface plasmon resonance imaging," Biosens. Bioelectron. **26**(2), 674–681 (2010).
10. J. Homola, and M. Piliarik, "SPR Sensor Instrumentation," in *Surface Plasmon Resonance Based Sensors* (Springer Berlin Heidelberg, 2006).
11. D. Evanko, "Label-free microscopy," Nat. Methods **7**(1), 36 (2010).
12. W. Wang, K. Foley, X. Shan, S. Wang, S. Eaton, V. J. Nagaraj, P. Wiktor, U. Patel, and N. Tao, "Single cells and intracellular processes studied by a plasmonic-based electrochemical impedance microscopy," Nat. Chem. **3**(3), 249–255 (2011).
13. S. Milgram, S. Cortes, M.-B. Villiers, P. Marche, A. Buhot, T. Livache, and Y. Roupioz, "On chip real time monitoring of B-cells hybridoma secretion of immunoglobulin," Biosens. Bioelectron. **26**(5), 2728–2732 (2011).
14. M. Horii, H. Shinohara, Y. Iribe, and M. Suzuki, "Living cell-based allergen sensing using a high resolution two-dimensional surface plasmon resonance imager," Analyst. **136**(13), 2706–2711 (2011).
15. P. K. Chattopadhyay, T. M. Gierahn, M. Roederer, and J. C. Love, "Single-cell technologies for monitoring immune systems," Nat. Immunol. **15**(2), 128–135 (2014).
16. B. Huang, F. Yu, and R. N. Zare, "Surface plasmon resonance imaging using a high numerical aperture microscope objective," Anal. Chem. **79**(7), 2979–2983 (2007).
17. L. Berguiga, S. Zhang, F. Argoul, and J. Elezgaray, "High-resolution surface-plasmon imaging in air and in water: V(z) curve and operating conditions," Opt. Lett. . **32**(5), 509–511 (2007).
18. E. Boyer-Provera, A. Rossi, L. Oriol, C. Dumontet, A. Plesa, L. Berguiga, J. Elezgaray, A. Arneodo, and F. Argoul, "Wavelet-based decomposition of high resolution surface plasmon microscopy V (Z) curves at visible and near infrared wavelengths," Opt. Express **21**(6), 7456–7477 (2013).
19. H. E. de Bruijn, R. P. H. Kooyman, and J. Greve, "Surface plasmon resonance microscopy: improvement of the resolution by rotation of the object," Appl. Opt. **32**(13), 2426–2430 (1993).
20. C. E. H. Berger, R. P. H. Kooyman, and J. Greve, "Resolution in surface plasmon microscopy," Rev. Sci. Instrum. **65**(9), 2829–2836 (1994).
21. K. F. Giebel, C. Bechinger, S. Herminghaus, M. Riedel, P. Leiderer, U. Weiland, and M. Bastmeyer, "Imaging of Cell/Substrate Contacts of Living Cells with Surface Plasmon Resonance Microscopy," Biophys. J. **76**(1), 509–516 (1999).
22. A. Peterson, M. Halter, A. Tona, K. Bhadriraju, and A. Plant, "Surface plasmon resonance imaging of cells and surface-associated fibronectin," BMC Cell Biology **10**(16), 1–17 (2009).
23. E. Suraniti, E. Sollier, R. Calemczuk, T. Livache, P. N. Marche, M.-B. Villiers, and Y. Roupioz, "Real-time detection of lymphocytes binding on an antibody chip using SPR imaging," Lab. Chip **7**(9), 1206–1208 (2007).
24. R. Bombera, L. Leroy, T. Livache, and Y. Roupioz, "DNA-directed capture of primary cells from a complex mixture and controlled orthogonal release monitored by SPR imaging," Biosens. Bioelectron. **33**(1), 10–16 (2012).
25. D. M. Bruls, T. H. Evers, J. A. H. Kahlman, P. J. W. van Lankvelt, M. Ovsyanko, E. G. M. Pelssers, J. J. H. B. Schleipen, F. K. de Theije, C. A. Verschuren, T. van der Wijk, J. B. A. van Zon, W. U. Dittmer, A. H. J. Immink, J. H. Nieuwenhuis, and M. W. J. Prins, "Rapid integrated biosensor for multiplexed immunoassays based on actuated magnetic nanoparticles," Lab. Chip **9**(24), 3504–3510 (2009).
26. J. Hulme, C. Malins, K. Singh, P. R. Fielden, and N. J. Goddard, "Internally-referenced resonant mirror for chemical and biochemical sensing," Analyst. **127**(9), 1233–1236 (2002).
27. W. Kong, Z. Zheng, Y. Wan, S. Li, and J. Liu, "High-sensitivity sensing based on intensity-interrogated Bloch surface wave sensors," Sens. Actuator B-Chem. **193**, 467–471 (2014).
28. W. N. Hansen, "Electric Fields Produced by the Propagation of Plane Coherent Electromagnetic Radiation in a Stratified Medium," J. Opt. Soc. Am. **58**(3), 380–388 (1968).
29. X. Zhang, and L. Hu, "Estimating scattering of pure water from density fluctuation of the refractive index," Opt. Express **17**(3), 1671–1678 (2009).
30. A. Vial, and T. Laroche, "Description of dispersion properties of metals by means of the critical points model and application to the study of resonant structures using the FDTD method," J. Phys. D: Appl. Phys. **40**(22), 7152 (2007).
31. A. D. Rakic, A. B. Djurisic, J. M. Elazar, and M. L. Majewski, "Optical Properties of Metallic Films for Vertical-Cavity Optoelectronic Devices," Appl. Opt. **37**(22), 5271–5283 (1998).
32. J. Vrs, "The Density and Refractive Index of Adsorbing Protein Layers," Biophys. J. **87**(1), 553–561 (2004).
33. S. K. Y. a. W. Tang, G.M., "Basic Microfluidic and Soft Lithographic Techniques," in *Optofluidics: Fundamentals, Devices and Applications*, D. P. P.L.F.L., and C.Y., Eds., ed. (McGraw-Hill, 2010).
34. T. Wilkop, Z. Wang, and Q. Cheng, "Analysis of Micro-Contact Printed Protein Patterns by SPR Imaging with a LED Light Source," Langmuir **20**(25), 11141–11148 (2004).
35. L. Grosjean, B. Cherif, E. Mercey, A. Roget, Y. Levy, P. N. Marche, M.-B. Villiers, and T. Livache, "A polypyrrole protein microarray for antibody-antigen interaction studies using a label-free detection process," Anal. Biochem. **347**(2), 193–200 (2005).
36. P. Guedon, and Y. Levy, "Method for characterising a surface, and device therefor," WO 2002048689.
37. E. Maillart, "Surface plasmon resonance imaging for simultaneous analysis of multiple biomolecular interactions

#214954 - $15.00 USD Received 27 Jun 2014; revised 22 Aug 2014; accepted 22 Aug 2014; published 11 Sep 2014

in real time," PhD thesis, Universite Paris Sud (2004).
38. F. Pillet, C. Thibault, S. Bellon, E. Maillart, E. Trevisiol, C. Vieu, J. M. Francois, and V. A. Leberre, "Simple surface chemistry to immobilize DNA probes that significantly increases sensitivity and spots density of surface plasmon resonance imaging based microarray systems," Sens. Actuator B-Chem. **147**(1), 87–92 (2010).
39. S. B. Ippolito, B. B. Goldberg, and M. S. Ünlü, "Theoretical analysis of numerical aperture increasing lens microscopy," J. Appl. Phys. **97**(5), 053105 (2005).
40. K. Yamamoto, K. Osato, I. Ichimura, F. Maeda, and T. Watanabe, "0.8-numerical-aperture two-element objective lens for the optical disk," Jpn. J. Appl. Phys. **36**(1B), 456–459 (1997).
41. T. Scheimpflug, "Improved method and apparatus for the systematic alteration or distortion of plane pictures and images by means of lenses and mirrors for photography and for other purposes," US 751347 (1904).
42. T. M. Chinowsky, M. S. Grow, K. S. Johnston, K. Nelson, T. Edwards, E. Fu, and P. Yager, "Compact, high performance surface plasmon resonance imaging system," Biosens. Bioelectron. **22**(9-10), 2208–2215 (2007).
43. E. M. Yeatman, "Resolution and sensitivity in surface plasmon microscopy and sensing," Biosens. Bioelectron. **11**(6-7), 635–649 (1996).
44. L. S. Jung, C. T. Campbell, T. M. Chinowsky, M. N. Mar, and S. S. Yee, "Quantitative interpretation of the response of surface plasmon resonance sensors to adsorbed films," Langmuir **14**(19), 5636–5648 (1998).
45. E. Wijaya, C. Lenaerts, S. Maricot, J. Hastanin, S. Habraken, J.-P. Vilcot, R. Boukherroub, and S. Szunerits, "Surface plasmon resonance-based biosensors: From the development of different SPR structures to novel surface functionalization strategies," Curr. Opin. Solid. St. M. **15**(5), 208–224 (2011).
46. L. Mondani, Y. Roupioz, S. Delannoy, P. Fach, and T. Livache, "Simultaneous enrichment and optical detection of low levels of stressed Escherichia coli O157:H7 in food matrices," J. Appl. Microbiol. **117**(2), 537–546 (2014).
47. Z. Wang, I. S. Chun, X. Li, Z.-Y. Ong, E. Pop, L. Millet, M. Gillette, and G. Popescu, "Topography and refractometry of nanostructures using spatial light interference microscopy," Opt. Lett. **35**(2), 208–210 (2010).
48. B. Liu, S. Li, and J. Hu, "Technological advances in high-throughput screening," Am. J. Pharmacogenomics **4**(4), 263–276 (2004).
49. P. N. Abadian, N. Tandogan, J. J. Jamieson, and E. D. Goluch, "Using surface plasmon resonance imaging to study bacterial biofilms," Biomicrofluidics **8**(2), 021804 (2014).

1. Introduction

Surface Plasmon Waves (SPW) represent the collective oscillation of electrons at a metal/dielectric interface and were first observed by Wood in 1902 [1]. In 1968, Otto and Kretschmann demonstrated that they can be optically generated using a glass substrate coupling [2, 3]. At a precise wavelength and incident angle, a strong and steep absorption occurs and is called Surface Plasmon Resonance (SPR). This resonance is highly sensitive to any refractive index change of the dielectric medium within a penetration depth called L_z, typically a few hundred nm [4]. This localized sensitivity emphasizes the effect of molecular adsorption/recognition.

SPR has become one of the major label-free an real-time techniques to monitor the kinetics of biomolecule interactions in aqueous environments [5]. More recently, analyses on living cells have emerged as a new challenge for SPR, which has been used in fundamental research to address cell biology issues [6, 7], as well as in the health and food industry where it has also demonstrated the ability to rapidly detect bacteria at low concentrations in complex and turbid media [5, 8].

For these applications, imaging the surface of the biochip is essential to measure a cells' SPR signal, position or morphology [9]. SPR imaging (SPRi) can be achieved by using a microscope objective or a prism to couple light and SPW [10]. Unlike labeling methods, SPRi preserves the integrity of the cells while allowing the observation of extra-and intracellular processes in real-time [11–14].

The intrinsic heterogeneity of living microorganisms makes it crucial to obtain statistical data by simultaneously monitoring a large number of individual cells [15]. This implies that the imaging technique must exhibit a high spatial resolution to clearly distinguish each cell from its neighbor, and a wide field-of-view (FOV) to observe as many cells as possible.

Objective-based SPRi has been subject to significant improvements on spatial resolution [16–18], but remains restricted to FOVs smaller than 100×100 μm^2 and cannot image more

#214954 - $15.00 USD Received 27 Jun 2014; revised 22 Aug 2014; accepted 22 Aug 2014; published 11 Sep 2014

than a few cells. In prism-based SPRi, there is no limitation on FOV, but spatial resolution is significantly lower, especially parallel to the SPW. This anisotropy is usually assigned to the propagation length L_x [19, 20]. However, in water environments, blur and distortion still exist at short wavelengths, where L_x should not be notable anymore [21–24], thereby suggesting an optical aberration phenomenon.

The present manuscript focuses on aberration analysis and reveals the basic mechanisms of spatial resolution and image formation in prism-based imaging techniques. It is applied to SPR, but can be easily extended to other techniques such as Frustrated Total Internal Reflection [25], Resonant Mirror [26] and Bloch Surface Wave [27].

Optimal SPRi prisms for biosensing are described in terms of apex angle, refractive index, metal coating and wavelength. We report a significant improvement on spatial resolution and FOV. As from now, prism-based SPRi appears as the only real-time label-free imaging method that combines large FOV (several mm^2), high sensitivity (monolayer of biomolecules) and high spatial resolution (1.7 to 5 μm).

2. Method

2.1. Numerical simulation

SPR curves and sensitivities are calculated with Mathematica 8.0 (Wolfram Research) using the matrix formalism for stratified media of ref. [28] considering a perfectly monochromatic and collimated illumination, and plane interfaces. The sensitivity optimization is performed with the NMaximize function. The same program is used to calculate the geometrical optics values. Literal expressions with respect to the wavelength (λ) are used for the refractive indices of pure water $n_d(\lambda)$ [29] and prism glass $n_p(\lambda)$ (N-BK7, SF11 and N-SF66 from Schott datasheets), and for the permittivity of metals $\varepsilon_m(\lambda)$ [30, 31]. Pure water is used for the dielectric as an approximation of saline buffer medium in biosensing applications. These continuous functions give an accurate estimation of various plasmonic properties in the visible spectrum. Results presented for gold take into account the constant 2-nm-thick adhesion layer of chromium present on our prisms. The optical indices of microorganisms and adsorbed biomolecule layers range from 1.36 to 1.55 [32]. In the present work, we set it at a mean value of n_{bio} = 1.41, which is also the one of PDMS [33]. Equations used to calculate L_x and L_z are the ones of ref. [4].

2.2. Experimental

Two types of prisms were used for high resolution imaging: SF11 prisms with an apex angle of 74° and N-SF66 prisms with an apex angle of 83° (Schott, Switzerland). Both are 12-mm-wide. 2 nm of chromium and 53 nm of gold were deposited by evaporation on prism bases. Commercial Horiba Scientific prisms (SF11, A_p=32°) were used as prisms optimized for very-wide-FOV. SPR images were taken on a 4 MP CMOS sensor (ORCA 4.0, Hamamatsu) or a 1.4 MP CCD sensor (pike 145B, Allied Vision Technologies), and cropped to display relevant features. Bright-field images were taken on a color 18 MP CMOS sensor (Canon 600D) mounted on an up-right Olympus microscope (BXFM-F) placed above the SPRi set-up. Light sources were fiber-coupled high-power LEDs M625F1 and M735F1 (Thorlabs). Spectral distributions have a Gaussian-shape with central wavelengths of 632 and 721 nm and a standard-deviation of 9.2 and 19.7 nm, respectively. The output of a 400-μm-wide optical fiber was collimated by a 25-mm-wide aspheric achromatic lens of focal length 35 mm. The beam then was passed through a linear polarizer to obtain transverse magnetic polarized light. The external angle of resonance with gold-coated SF66 prisms was measured at 49° at λ = 632 nm and 46° at λ = 721 nm. At these wavelengths, the internal or external angles of maximal sensitivity θ_{SPRi} are about 1° lower. In classic imaging mode, the angle of the imaging system was 21° at λ = 632 nm. Image sequences of line-scan imaging mode were obtained by displacing the whole

#214954 - $15.00 USD Received 27 Jun 2014; revised 22 Aug 2014; accepted 22 Aug 2014; published 11 Sep 2014

imaging system and camera at a constant speed with a motorized stage and by taking images at a constant rate. These images were then realigned using the ImageJ plugin Stackreg to correct small lateral shifts due to imperfect optical alignment, and finally processed by Mathematica to juxtapose all the clear strips together.

Images of Figs. 1(a') and 1(b') and Fig. 6(b) were taken with a 20× LMPLFLN Olympus objective (NA = 0.4) and a tube lens focal length of 200 mm. Images of Figs. 1(c) and 4 were taken with a 50× LMPLFLN Olympus objective (NA = 0.5) and a tube lens of 65 mm and 200 mm, respectively. Images of Figs. 5(a) and 5(b) were taken with a 4× Edmund Optics objective (NA = 0.1) and a tube lens of 100 mm. Image of Fig. 5(c) was taken with a high NA aspheric lens of focal length 18.75 mm (NA = 0.66) and a tube lens of 100 mm. Image of Fig. 6(d) was taken with a 50× LMPLFLN Olympus objective (NA = 0.5) with a tube lens of 200 mm. Bright-field images of Figs. 6(a), 6(c) and 6(e) were taken with a 20× LMPLFLN Olympus objective. SPR and bright-field images of Figs. 7(a) and 7(a'), 7(b) and 7(b'), and 7(c) and 7(c') were obtained with a 4× Edmund Optics objective (NA = 0.1), a 10× (NA = 0.25) and a 20× (NA = 0.4) LMPLFLN Olympus objective, respectively, and a tube lens of 200 mm (SPR images).

Jurkat E6.1 cells are human T lymphocytes that grow as single-cell suspensions with an average diameter of 15 μm. They were purchased from ATCC and were cultivated at concentrations from 0.25 to 1.5×10^6/mL at 37°C and 5% CO_2 in RPMI 1640 medium, GlutaMAX^{TM} Supplement, HEPES (Gibco) supplemented by 10% FBS (PAA) and 1% penicillin-streptomycin (10,000 μg/mL) (Gibco). In order to anchor the cells onto the surface of the biochip, antibodies specific for CD3 cell markers were grafted with polypyrrole and spotted (≈500 μm-wide) by electrochemistry as previously described in [35] by Grosjean *et al.*. The prism surface was then kept in PBS 1× (Sigma-Aldrich) to prevent drying of the antibody spots. A drop of Jurkat cells suspension in RPMI (≈200 μl) at a concentration of 2.5×10^6/mL was deposited on the prism. Images were taken after 10 min. The rinsing step was achieved by adding 5 drops of medium on the inclined prism surface.

Staphylococcus epidermidis are 1-μm-wide bacteria which are naturally present on human skin. They were purchased from ATCC (strain 12228) and were cultivated at 37°C in TSB medium (Sigma-Aldrich) until they reached a concentration of 1.0×10^7/mL. In order to bind the bacteria to the gold surface, the prism was incubated overnight with poly-L-Lysine (Sigma-Aldrich, Mol. Wt. 150,000 - 300,000) at 0.01% and rinsed with deionized water. Without this surface chemistry, bacteria were not close enough to the gold to be observed in SPR (data not shown). A drop of bacterial suspension in TSB was then incubated during 1 hour, and softly rinsed with TSB. Finally, the sample was covered by a coverslip to allow optical microscopic observations.

Micro-patterned PDMS (Sylgard 184) stamps were fabricated by replicating a previously silanized silicon wafer mold. The mold was fabricated by standard deep-UV photolithography followed by Reactive Ion Etching, and exhibits various 4.4-μm-high patterns with lateral dimensions down to 2 μm. Surface-Enhanced-Ellipsometric-Contrast microscopy performed with $T-SiO_2$ Surfs (Nanolane, France) reveals that the contact area of the smallest cylindrical PDMS pillars with gold is less than 1-μm-wide. Some of these smallest features were missing on the mold and on SPR images. All measurements and images of PDMS stamps were performed at room temperature in deionized water.

#214954 - $15.00 USD Received 27 Jun 2014; revised 22 Aug 2014; accepted 22 Aug 2014; published 11 Sep 2014

3. Geometrical aberrations and optimized configurations in prism-based SPRi

When SPRi is performed on isosceles prisms illuminated by a collimated beam of light (main rays), the angles of illumination and reflection (internal or external) are equal. Here, we refer to the angles that maximize the sensitivity as $\theta_{SPRi-int}$ and $\theta_{SPRi-ext}$ as depicted in Fig. 1(a).

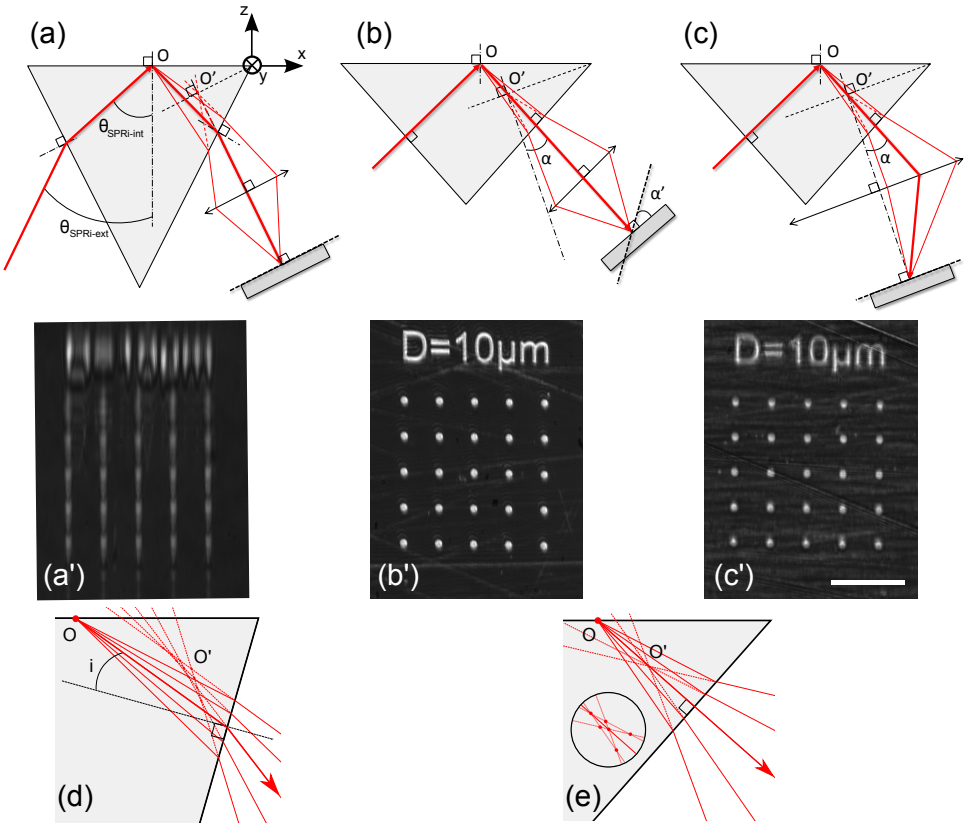

Fig. 1. Prism-based SPRi optical configurations and geometrical aberrations illustration with corresponding small-FOV SPR images of 10-µm-wide PDMS pillars in water on gold-coated SF11 prisms. (a and a') Classic imaging mode with a prism optimized for very-wide-FOV: the virtual image is normal to the main ray which is parallel to the optical axis, α=0°. (b and b') Line-scan imaging mode with prism optimized for resolution: the out face is normal to the main ray which is parallel to the optical axis. The image is reconstructed from 100 strips. (c and c') Classic imaging mode with prism optimized for resolution: the out face is normal to the main ray, the optical axis is normal to the virtual image. (d and e) Geometrical aberration illustration at a plane interface for main ray with an angle of incidence i≠0 and i=0 (zoom in the inset). Scale bar: 100 µm.

In a basic imaging system, the final image of a plane object is also a plane that coincides with the camera sensor. The easiest way to achieve this is to place the optical axis of the imaging system normal to the object plane. In the case of prism-based imaging, refraction by the out face deviates the rays and creates a virtual image of the base into the prism, which corresponds to the object plane of the imaging system. Moreover, spherical and coma aberrations of the imaging system are minimized when rays are almost parallel to the optical axis and pass through the center part of the lenses. This condition can be fulfilled in SPRi by correctly selecting the refractive index and the apex angle of the prism so the external main rays are perpendicular

#214954 - $15.00 USD Received 27 Jun 2014; revised 22 Aug 2014; accepted 22 Aug 2014; published 11 Sep 2014

to the virtual image plane, i.e α = 0°, as depicted in Fig. 1(a) [36, 37]. This configuration is optimized to observe very-wide-FOV with simple and inexpensive optics, and enables the simultaneous monitoring of more than a thousand spots over surfaces as large as 1 cm^2 [38]. However, refraction at the out face of the prism generates geometrical aberrations that strongly alter lateral resolution.

Even if the prism base is illuminated by a collimated beam of light, the reflection is not perfectly specular, otherwise imaging would not be possible. This diffuse reflection creates spherical waves which correspond to secondary rays. The secondary rays coming from a single point source O do not strike the out face with the same angle of incidence. As a consequence, the virtual image of O is not a point but a spread spot O' as it is pointed out by ray tracing in Fig. 1(d). This spreading increases with respect to the incident angle, the refractive index of the prism n_p, the angular diffusion of O and the thickness of the glass [39]. This thickness is proportional to the distance d between the point source O and the imaging side edge of the prism. The optical response is not of spherical symmetry and explains the deformation and artifacts visible on small patterns.

For prisms optimized for very-wide-FOV, the impact of O angular diffusion can be decreased by diaphragming the imaging system. Obviously, a trade-off must be achieved as the resolution of the imaging system also decreases with the numerical aperture (NA). The apex angle of such prisms can then be calculated by considering angular diffusion close to zero, as presented in Table 1. A negative apex angle prism corresponds to a truncated prism whose base is facing down and the metal-coated surface is the truncated plane, while for A_p = 0°, the section of the prism is a rectangle.

Table 1. Apex angles at +/- 0.5° for 50-nm-gold-coated-prisms of refractive index from 1.5 to 2.0 at λ = 632 nm in water and calculated at an angular diffusion of +/- 0.1° around $\theta_{SPRi-int}$. Corresponding internal and external angles of maximal sensitivity.

n_p	1.5	1.6	1.7	1.8	1.9	2.0
A_p resolution	34	52	65	74	82	88
A_p very-wide-FOV	-33.5	-1.5	21.0	38.0	52.0	62.5
$\theta_{SPRi-int}$	73.0	64.0	57.5	53.0	49.0	46.0
$\theta_{SPRi-ext}$	50.5	44.5	40.0	37.0	34.5	32.5

These aberrations can be minimized by choosing the apex angle so that the angles of incidence on the out face remain close to zero, i.e. $\theta_{SPRi-ext} = \theta_{SPRi-int}$ (Fig. 1(e)). This configuration is equivalent to the one encounter in subsurface microscopy, where geometrical aberrations can be approximated by spherical aberrations. Solutions such as Numerical Aperture Increasing Lens [39] or aspheric lenses [40] can compensate the remaining aberrations for a particular object depth, but restrict imaging to a narrow region of the prism. For prisms optimized for resolution, the minimal thickness of glass crossed by the light coming from a point source O is equal to $d \times \sin(A_b)$, where A_b is the base angle of the prism. As spherical aberrations are proportional to the glass thickness crossed, they can be neglected as the object gets closer to the prism edge ($d \longrightarrow 0$ mm). Minimization of geometrical aberrations is satisfied for $Ap = \pi - 2 \times \theta_{SPRi-int}$ and leads to $\alpha = \arctan\left[\tan\left(\theta_{SPRi-int}\right)/n_p\right]$. Note that changing the apex angle only affects the resolution in the X-axis.

Two optical schemes can then be envisaged. In the first one (Fig. 1(b)), the optical axis is parallel to the main rays. This configuration leads to the theoretical highest resolution achievable in prism-based imaging because optical aberrations of the prism and the imaging system are minimized. Moreover, there is no limitation on magnification or FOV. In this case, external

#214954 - $15.00 USD Received 27 Jun 2014; revised 22 Aug 2014; accepted 22 Aug 2014; published 11 Sep 2014

main rays are not perpendicular to the virtual image plane and the final image is inclined by an angle α' with respect to the normal of the optical axis (Scheimpflug principle [41]), meaning that only a line can be in focus on the camera sensor. Due to the non-zero depth-of-field of the imaging system, this line is a strip and the entire surface can be imaged in line-scan imaging mode, i.e. by sequentially adjusting the focus and juxtaposing all these clear strips into a final image.

In the second configuration shown in Fig. 1(c), the axis of the imaging system is normal to the virtual image so that the final image coincides with the camera sensor plane (classic imaging mode). In this case, the NA of the imaging system has to be sufficient to capture the main rays arriving with an angle α, that is to say $NA_{min} \geq sin(\alpha)$. But the higher the angle α, the higher the coma aberrations. This angle can however be lowered by increasing n_p, which also has the benefit to decrease the anamorphose. These aberrations can also be significantly decreased by designing a corrected imaging system [42].

4. Geometrical aberrations estimation

Tendency of the geometrical aberrations as a function of the apex angle A_p and refractive index n_p can be evaluated in a first approximation by considering the spreading of the virtual spot O within the virtual image plane. Thus, this plane has to be precisely defined using three conditions. First, it is perpendicular to the XZ plane. Then, it passes by the imaging side edge of the prism. Finally, it passes by the effective virtual intersection point O'$_m$ of the external rays. If we do not take into consideration the non-infinite depth-of-field of the imaging system and limit the analysis to the XZ plane, O'$_m$ can be approximated by the mean position of all ray intersection points O' (Fig. 2). The number of O' points is equal to the combination of 2 among N rays: $C_N^2 = \frac{N!}{2!\times(N-2)!}$.

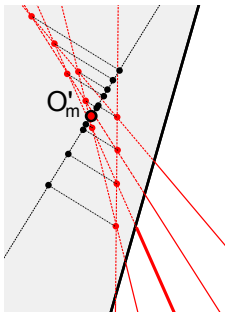

Fig. 2. Schematic representation of the projection of O' virtual points onto the virtual image plane that passes by the mean intersection point O'$_m$.

The spreading is finally measured by the standard deviation σ of O' points projected onto this virtual image plane. The dimension of σ is a length which is proportional to d. For comparison purposes, we normalize it by its minimal value among all simulations to express the relative standard deviation σ_r. Herein, we consider 41 equally spaced rays (= 820 points) to represent a point source having an angular diffusion around $\theta_{SPRi-int}$ that gives a resolution limit by the Rayleigh criterion of 1.5 µm at λ = 632 nm. Table 2 summarizes these results for N-BK7 (n=1.52), SF11 (n=1.78) and N-SF66 (n=1.91) gold-coated prisms with angular diffusion of +/- 9.6°, +/- 8.2° and +/- 7.6°, respectively. The corresponding internal and external angles θ_{SPRi} are given in Table 3. The higher the n_p, the lesser the loss of resolution with respect to A_p, and the lesser the minimal NA required for classic imaging mode at apex angles optimized for resolution. A trade-off between coma aberrations of the imaging system and geometrical

#214954 - $15.00 USD Received 27 Jun 2014; revised 22 Aug 2014; accepted 22 Aug 2014; published 11 Sep 2014

Table 2. Optical parameters of prism-based SPRi at $\lambda = 632$ nm in water for different prism glasses. A_p is given in degrees.

Configuration	N-BK7			SF11			N-SF66		
	A_p	NA_{min}	σ_r	A_p	NA_{min}	σ_r	A_p	NA_{min}	σ_r
Very-wide-FOV	-24.0	-	37.6	37.0	-	17.3	54.5	-	11.5
Resolution	38.0	0.88	1.32	73.0	0.58	1.18	83.0	0.48	1

Table 3. $\theta_{SPRi-int}$ and $\theta_{SPRi-ext}$ at +/- 0.5° for 50-nm-gold-coated-prisms optimized for very-wide-FOV at λ = 632 nm in water.

θ_{SPRi}	N-BK7	SF11	N-SF66
int	71.0	53.5	48.5
ext	51.0	38.0	35.0

aberrations of the prism could also be found by choosing an apex angle between the two optimized configurations. In air environments with N-BK7 prisms, $\theta_{SPRi-int}$= 43.5°, which means a resolution-optimized apex angle of 93°. This is certainly the reason why geometrical aberrations were omitted in previous studies [20]. By comparing the minimum standard deviations, we can also conclude that higher refractive index prisms generate less spherical aberrations and offer better ultimate resolution. However, for technical reasons such as prism matter, oil-coupling, or accessible angles, it may be interesting to use lower refractive index glasses (Table 1). As a conclusion, high n_p is better for all prism-based SPRi configurations.

5. Trade-off between L_x and sensitivity

In this section we conduct a general analysis on the propagation length L_x and sensitivity over the visible spectrum for the metals commonly used in SPRi : gold, silver, aluminum and copper. In SPRi, the fact that the propagation length L_x limits the spatial resolution in the propagation direction is a well known issue. As plotted in Fig. 3(a), L_x increases with respect to the wavelength for these metals. The spatial resolution can then be improved by decreasing the wavelength of excitation [20], or, at a given wavelength, by choosing a metal which presents a smaller L_x [16, 21]. However, in both cases, the improvement of resolution also influences the sensitivity. Our goal is to establish which metal exhibits the better trade-off for high resolution imaging in biosensing, that is to say which exhibits a reasonable sensitivity for biosensing and low L_x. Therefore, we need to plot the sensitivity as a function of L_x.

In intensity-modulation, the SPR sensitivity is usually quantified as the increase of reflectivity with respect to the increase of the dielectric refractive index: $\partial R/\partial n_d$, and expressed in %/RIU (refractive index unit). But this convention does not take into account the penetration depth L_z of the SPW into the dielectric. From the optical point-of-view, a biorecognition process is equivalent to the adsorption of a homogenous biolayer of a given thickness h on the metal. As shown by Jung *et al.* [44], the effective refractive index of the dielectric n_{eff} (the one "felt" by the SPW) for a biolayer of refractive index n_{bio} and thickness h depends on L_z and is given by $n_{eff} = n_d + (n_{bio} - n_d) \times \{1 - \exp[-h/(2 \times L_z)]\}$. As shown in Fig. 3(b), L_z varies up to a factor of 3 for gold and copper, and 6 for silver and aluminum in the visible range. Thus, the increase of effective refractive index $\Delta n_{eff} = n_{eff} - n_d$ due to a given biorecognition process also depends on λ. As a consequence, the latter convention is not the more appropriate

#214954 - $15.00 USD Received 27 Jun 2014; revised 22 Aug 2014; accepted 22 Aug 2014; published 11 Sep 2014

way to evaluate the SPR sensitivity in biosensing. Hence, it appears more relevant to determine the sensitivity as the increase of reflectivity ΔR (%) due to the adsorption of a biolayer of a constant thickness h and refractive index $n_{bio} = 1.41$.

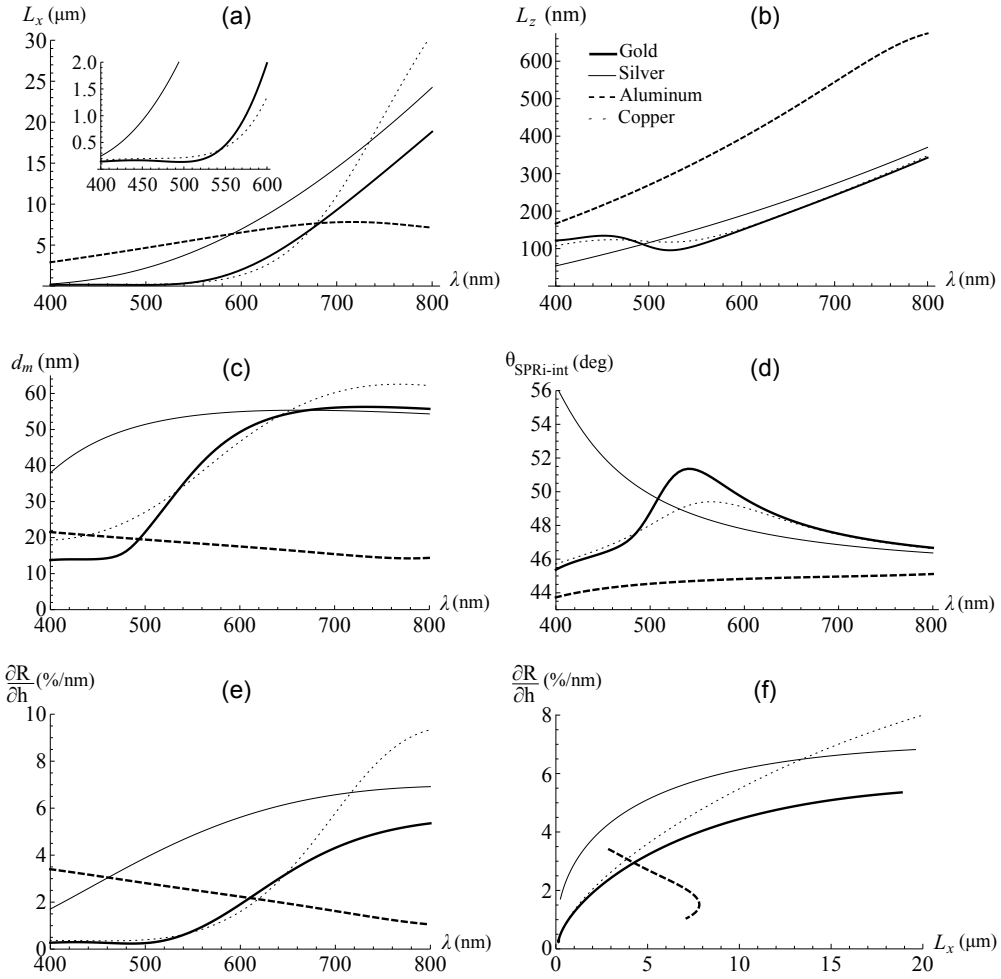

Fig. 3. Plasmonic properties at the metal/water interface over the visible spectrum. (a) Propagation length L_x. (b) Penetration depth L_z. (c) Optimal thickness of metal. (d) Internal angle of maximal sensitivity $\theta_{SPRi-int}$. (e) Sensitivity. (f) trade-off visualization: sensitivity with respect to L_x.

To go further, at each wavelength, the metal thickness can be optimized to maximize ΔR. Since ΔR also depends on the internal angle of incidence, the results of the maximization are a couple of optimized parameters $\{d_m, \theta_{SPRi-int}\}$ and the corresponding sensitivity ΔR, where d_m is the optimal metal thickness and $\theta_{SPRi-int}$ the working angle. In the 400 - 800 wavelength range, our calculations show that ΔR is proportional to h for $h \leq 5$ nm. Thus, by choosing a thickness $h = 1$ nm in the optimization process, the calculated ΔR is also equal to $\partial R/\partial h$ for thin biolayers, and the sensitivity can be expressed in %/nm. These optimized parameters are calculated at a step of 5 nm in wavelength (Figs. 3(c) and 3(d)) and lead to the optimized sensitivities presented in Fig. 3(e) (scatters not shown for the sake of clarity). Here, we show that the sensitivities of gold, silver and copper tend toward a plateau at high wavelength. Indeed,

#214954 - $15.00 USD Received 27 Jun 2014; revised 22 Aug 2014; accepted 22 Aug 2014; published 11 Sep 2014

by extending the wavelength range, it can even be shown that gold reaches a maximum of 5.6 %/nm at λ = 895 nm, silver reaches a maximum of 6.9 %/nm at λ = 835 nm, while for copper the maximum is 9.4 %/nm at λ = 825 nm. Surprisingly, the sensitivity of aluminum decreases with respect to λ. We emphasize that the spectral and angular dispersion of the light source and the roughness of the interface, which depends on the experimental set-up, were not taken into account in these simulations. Their effect would be to reduce the sensitivity [34].

At each wavelength of the optimization process, we have a couple $\lambda \rightarrow \{L_x, \Delta R\}$. The trade-off can then be visualized by plotting ΔR with respect to L_x, as presented in Fig. 3(f), where silver appears as the best metal, whatever the wavelength. For L_x lower than 1.5 μm, gold and copper are equivalent ($\lambda \leq$ 590 nm for gold and 605 nm for copper), after which the trade-off achieved by copper is significantly better as L_x increases (and thus λ). Once again, the behavior of aluminum is singular compared to other metals since its sensitivity decreases as L_x increases (increasing λ). Nonetheless, it achieves a better trade-off than gold in the narrow range 2.9 μm $\leq L_x \leq$ 4.3 μm (400 nm $\leq \lambda \leq$ 480 nm). However, gold is by far the most convenient and used metal for SPR biosensors. Compared to the other metals, gold is stainless and stable in aqueous solutions, biocompatible, and can easily be functionalized by electrochemistry [35] or self-assembling of organic monolayers [45] to anchor the probe molecules.

6. Results and discussion

6.1. Spatial resolution measurements in SPRi

Microstructured PDMS stamps represent a simple, accurate and reproducible way to evaluate the image quality and resolution in SPRi. As presented below, FOV is also a key parameter for resolution, especially for classic imaging mode with prism optimized for resolution. We divided FOV into 4 categories: very-wide ($\geq$20 mm^2), wide ($\approx$6 mm^2), small ($\approx$0.7 mm^2) and very-small ($\leq$0.1 mm^2).

The lateral resolution of an optical instrument can be measured as the first zero of its Point-Spread-Function (PSF), which is the function that describes the intensity with respect to the distance when imaging a single point source. The PSF can be obtained experimentally by imaging objects with dimensions smaller than the spatial resolution. Herein, we use networks of PDMS pillars which enable us to know the exact distance d from the edge of the prism. The anisotropic shape of the response on Fig. 4 indicates that resolution in prism-based SPRi must be described by three values: the resolution perpendicular to the SPW and the resolutions parallel to the SPW both before the step of refractive index (X $\leq$ 0) and after the step (X $\geq$ 0); the latter being strongly affected by L_x.

Perpendicular to the propagation direction (Y axis), the experimental PSF was fitted with a Gaussian function. Parallel to the propagation direction (X axis), we also use a Gaussian function fit, but only before the refractive index step, that is to say in the negative X direction by starting at the highest intensity point. The resolution was then evaluated by the FWHM (Full Width at Half Maximum). Even with optimized prisms, resolution is still affected by spherical aberrations, as testified by the linear increase of FWHM with respect to d. With N-SF66 prisms, the ultimate resolution was found to be 1.7 μm perpendicular and 2.8 μm parallel to the SPW at d=0.2 mm, and respectively 2.6 and 5.0 μm at d=10.2 mm. These results are in good agreement with the resolution found in ref. [19,20]. We assume that L_x is also responsible for the lowering of the resolution in the propagation direction even before the step of refractive index (negative X direction). In fact, the optical signal parallel to the SPW is the convolution of 3 functions: the function that describes the geometry of the real object (a 1-μm-wide square function for instance), a decreasing exponential function of characteristic length L_x, and the PSF of the optical system. The fact that the experimental resolution perpendicular to the SPW is not as good as the one of our imaging system ($\approx$760 nm) at $d \longrightarrow$0 mm is attributed to the light

#214954 - $15.00 USD Received 27 Jun 2014; revised 22 Aug 2014; accepted 22 Aug 2014; published 11 Sep 2014

diffusion by the object itself, which is restricted to a small solid angle. This diffusion could be increased by using a focused illumination beam, but in SPR this would result in a complete loss of contrast and sensitivity.

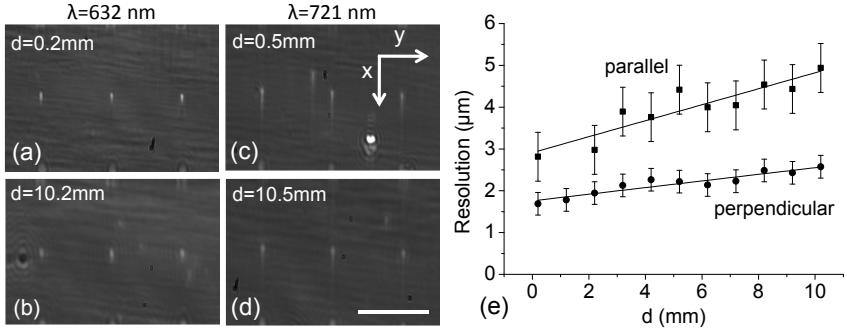

Fig. 4. Very-small-FOV SPR images of less than 1-μm-wide PDMS pillars in water at increasing distance *d* from the imaging side edge of the prism. SPW propagate downward. (a and b), at λ=632 nm. (c and d), at λ = 721 nm. Images were taken with a gold-coated N-SF66 prism (Ap = 83°) in the configuration of Fig. 1(b). (e) Resolution perpendicular and parallel (before the step) to the SPW with respect to the distance *d* at λ = 632 nm in water with a N-SF66 prism. Each point is an average of 1 to 3 PDMS pillars. The constant error bars are equal to the maximum difference observed for each orientation. Scale bar: 50 μm.

In view of the ultimate resolution, and taking into account that sensitivity is also a key parameter for biosensing, we selected λ = 632 nm as a reasonable trade-off between resolution and sensitivity.

6.2. SPR imaging of micro-structured PDMS stamps and living cells

Figures 1(a')-1(b') show a comparison for small-FOV between SF11 prisms optimized for very-wide-FOV and resolution. The highest image quality is obtained using the line-scan imaging mode (Fig. 1(b')). Classic imaging mode with prism optimized for resolution (Fig. 1(c')) exhibits a slightly lower resolution because of coma aberrations, but remains sufficient to clearly discriminate objects of only few μm (such as defects on the surface). Fig. 1(a') indicates how important geometrical aberrations are for spatial resolution in prism-based SPRi. This image shows that, in addition to deformation, artifacts appear for network patterns, such as the less intense line at the bottom of the image. For denser patterns, it becomes even impossible to count them, and such images should be interpreted with care, especially for resolution measurements. Here, at the best focus, we measure a resolution of 8 μm perpendicular and 30 μm parallel to the SPW.

Fig. 5 proposes the same comparison for larger FOV. Prisms optimized for very-wide-FOV offer relatively clear overall images, but magnification on small patterns reveals high deformation (Figs. 5(a) and 5(a')). As for small-FOV, the best results are obtained with the line-scan mode (Figs. 5(b) and 5(b')). In classic imaging mode, coma aberrations become more important due to the use of a simple high NA aspheric lens instead of a corrected microscope objective. Moreover, very-wide-FOV imaging requires the use of a small focal length tube lens that makes images more subject to field curvature and distortion aberrations. In our actual set-up, we limit this imaging mode to wide-FOV (Figs. 5(c) and 5(c')) which has a resolution of approximately 5 μm perpendicular and 20 μm parallel to the SPW.

#214954 - $15.00 USD Received 27 Jun 2014; revised 22 Aug 2014; accepted 22 Aug 2014; published 11 Sep 2014

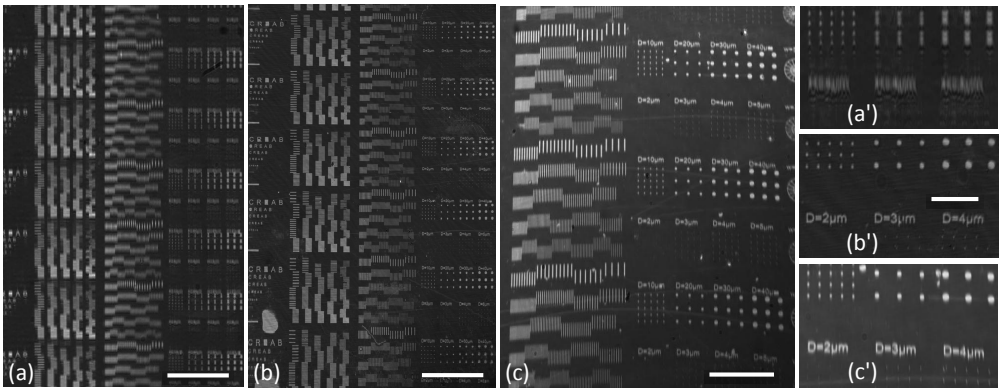

Fig. 5. Very-wide and wide-FOV SPR images of the micro-patterned PDMS stamp in water using gold-coated SF11 prism optimized for very-wide-FOV (a) (Ap = 32°) and N-SF66 prism optimized for resolution (b and c) (Ap = 83°). SPW travel upward. (a) Classic imaging mode in configuration of Fig. 1(a). (b) Line-scan imaging mode (100 strips) obtained in configuration of Fig. 1(b). (c) Classic imaging mode in configuration of Fig. 1(c). (a'- c') Corresponding magnifications on PDMS pillars of 30, 20, 10, 4, 3 and 2 µm diameters. Scale bars: 1 mm (a and b), 500 µm (c), 200 µm (a'- c').

In order to validate the performances of our set-up on real biological objects, we compare images of microorganisms obtained by high resolution prism-based SPRi and bright-field microscopy on Fig. 6. For the jurkat cells, Figs. 6(a) and 6(b) show that SPRi images provide information that bright-field microscopy cannot access, such as the direct observation of cell recognition by specific antibodies. Indeed, since SPR is only sensitive in the L_z range, which is 150 nm at λ = 632 nm, anchoring the cells to the gold surface with antibodies significantly increases their signal compared to bare gold sedimentation outside of the spot. Once rinsed, only the corresponding captured cells remain (Fig. 6(c)).

The imaging of individual microorganisms was also performed on *Staphylococcus epidermidis* (Figs. 6(d) and 6(e)). Even close bacteria are individually distinguished both perpendicular and parallel to the SPW. Their signal corresponds to the PSF of the SPRi set-up. However, because their diameter is only one micron, which is less than the spatial resolution, densely packed bacteria are observed as a single object with a signal higher than a single specimen. In the view of bacterial detection, having a multiplexed sensor with negative controls is indispensable and requires larger FOVs. In Fig. 7, we report FOV up to 4 mm^2 presenting several thousand bacterial signals.

High spatial resolution prism-based SPRi allows the measure of refractive index changes within and in the vicinity of several hundreds of individual cells, which presents great interest to dynamically investigate biological processes including shape, migration, growth and secretion. For prokaryote cells, this technique also shows a great potential to decrease both the assay time and the detection limit of a pathogenic bacterial identification by directly counting the binding events instead of the conventional intensity shift measurement [46].

#214954 - $15.00 USD Received 27 Jun 2014; revised 22 Aug 2014; accepted 22 Aug 2014; published 11 Sep 2014

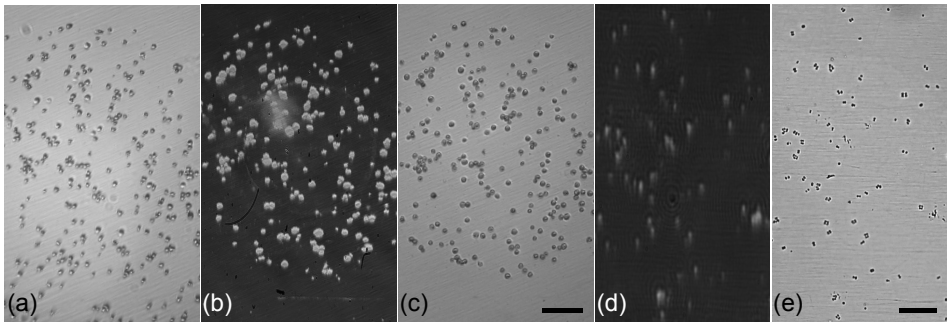

Fig. 6. Optical and SPR images of individual eukaryote cells (a - c) and bacteria (d and e) at λ = 632 mm. (a), Optical image before the rinsing step. Jurkat cells are randomly distributed. (b) Line-scan SPR image (40 strips) of the same spot before rinsing step. The extension of the anti-CD3-grafted-polypyrrole spot is clearly visible on the SPR images because anchored cells generate a signal much larger than the ones sedimented on bare gold. (c) Optical image after the rinsing step. Only captured cells remain. (d) Line-scan SPR image (70 strips) of *Staphylococcus epidermidis* attached to the gold surface by poly-L-Lysine. (e) Corresponding bright-field optical image. Individual bacteria are resolved when their respective separation is larger than the spatial resolution. Scale bars: 100 μm (a - c), 25 μm (d and e).

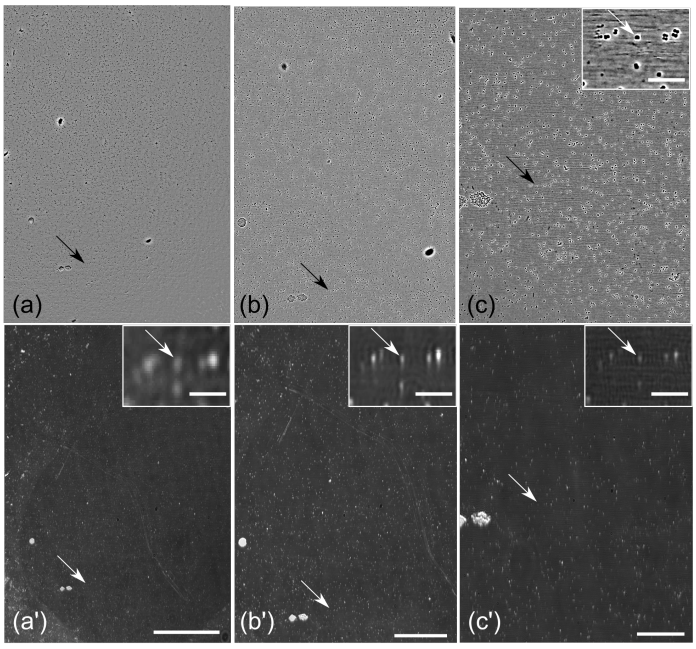

Fig. 7. Comparison between bright-field and line-scan imaging mode SPR images of bacterial signals on large field-of-views. (a and a') 4× objective, FOV=4.3 mm^2 The surface density of individual bacterial signals is about 1,900/mm^2, which leads to more than 8,000 detection on the entire image. (b and b') 10× objective, FOV=1.6 mm^2. (c and c') 20× objective, FOV=0.31 mm^2. Magnification on a single bacteria pointed by the arrow in the inset. Scale bars: 500 μm (a and a'), 250 μm (b and b'), 100 μm (c and c'), 20 μm (inset).

#214954 - $15.00 USD Received 27 Jun 2014; revised 22 Aug 2014; accepted 22 Aug 2014; published 11 Sep 2014

7. Conclusion

In this work, we have addressed the fundamental issue of spatial resolution and image formation in prism-based imaging techniques, and applied it to SPR. We have demonstrated that, in addition to plasmon decay length L_x, resolution is mainly governed by geometrical aberrations induced by the prism. Optimized gold-coated prisms have been designed to obtain the ultimate resolution of 1.7 μm perpendicular and 2.8 μm parallel to the SPW at λ = 632 nm in water on field-of-views as large as 20 mm^2. Resolution is ultimately limited by the light diffusion of the object itself and is linearly degraded due to spherical aberrations by a factor of 1.7/cm when increasing the distance of the object from the imaging side edge of the prism.

Due to its high surface sensitivity compared to conventional optical microscopy, high resolution prism-based SPRi offers the unique ability to monitor, in real-time and without any labeling, micrometer-size biochemical phenomenon on wide field-of-views. This imaging technique is particularly adapted to obtain biologically significant statistical data, such as extra and intracellular processes on large populations of individual living cells. Typical applications include studies on protein secretions for monitoring immune systems [15], neuronal network activity [47], high-throughput screening of drugs [48], growth of biofilms from a few bacteria [49], or high-performance pathogenic bacterial detection [8].

Acknowledgments

This work was partly supported by the ANR Multicell (2010-BLAN-1519-01), ANR Cellestim projects (2011-NANO-023-01), Labex Arcane supporting program (ANR-11-LABX-0003-01) and "Lyonbiopole" network. The authors thank Thierry Leïchlé and the Platform Micro and Nanotechnologies (LAAS-CNRS, Toulouse) for the fabrication of the photomask, and Dianne Pulido for discussions and proofreading.

#214954 - $15.00 USD Received 27 Jun 2014; revised 22 Aug 2014; accepted 22 Aug 2014; published 11 Sep 2014